Chemical Engineering Journal 435 (2022) 134864

Contents lists available at ScienceDirect

Chemical Engineering Journal

journal homepage: www.elsevier.com/locate/cej

Solar CO_2 hydrogenation by photocatalytic foams

Lourdes Hurtado [a,1,2], Abhinav Mohan [a,b,2], Ulrich Ulmer [a], Reyna Natividad [c], Athanasios A. Tountas [d], Wei Sun [a,e], Lu Wang [a], Boeun Kim [f], Mohini M. Sain [b,d], Geoffrey A. Ozin [a,*]

[a] Department of Chemistry, University of Toronto, 80 Saint George Street, ON, M5S 3H6, Toronto, Canada
[b] Department of Mechanical and Industrial Engineering, University of Toronto, 5 King's College Rd, ON, M5S 3G8, Toronto, Canada
[c] Chemical Engineering Laboratory, Centro Conjunto de Investigación en Química Sustentable, UAEM-UNAM, Universidad Autónoma del Estado de México, km 14 Carretera Toluca-Atlacomulco, 50200, Toluca, Mexico
[d] Department of Chemical Engineering and Applied Chemistry, University of Toronto, 200 College St, Toronto, ON M5S 3E5, Toronto, Canada
[e] School of Materials Science and Engineering, Zhejiang University, Hangzhou-310027, PR China
[f] Department of Chemical and Biological Engineering, The Department of Chemistry, University of Wisconsin-Madison, 1415 Engineering Dr, WI, 53706, Madison, USA

ARTICLE INFO

Keywords:
CO_2 reduction
Solar reverse water–gas shift
Defected indium oxide hydroxide
Metallic foams
Hybrid photocatalysis

ABSTRACT

Here we report the enhanced light penetration and mass transfer efficiency of photocatalytic foams to convert CO_2 to CO. The viability of utilizing a metallic foam as a model photocatalyst support is used to evaluate the photochemical and thermochemical reverse water gas shift reaction catalyzed by photoactive indium oxide hydroxide nanorods uniformly coated on nickel foams. A light-enhanced CO production rate up to 130% higher than the dark CO production was achieved through enhanced light penetration. A remarkably high thermochemical CO production rate of 0.75 mmol g_{cat}^{-1} h^{-1} was achieved at 295 °C. Whilst several approaches to optimization of photocatalyst morphology at the nanoscale have been successful in extending electron hole-pair lifetime and modifying the site of reactions, these advantages cannot be significantly realized unless microscale to macroscale structuring efforts, that shorten the path length for diffusion of the reactant gas molecule and lengthen photon penetration to these catalytic sites are integrated. The superior catalytic performance of the indium oxide hydroxide nanorods on an optimized coated foam configuration compared to the performance of packed bed and thin film configurations demonstrates the critical importance of using structured supports in scale up of future photocatalytic processes.

1. Introduction

Technologies for the photocatalytic transformation of gaseous carbon dioxide (CO_2) to synthetic fuels and value added chemicals have received increasing attention in recent years [1-4]. To achieve technological readiness, the efficiency of these photocatalytic processes needs to be significantly boosted through the design of innovative catalyst architectures and reactor configurations, that allow efficiently capture and utilization of light by the catalyst. Thin films of photocatalytic materials could serve this purpose by optimizing the penetration of light to the maximum number of photoactive catalyst sites, however implementation in practice would require inordinately large areas of land. Proposed herein is a more practical solution to this problem using photocatalytic foams. Their millimeter scale pores permit light incident on the surface of the foam to penetrate throughout the entire volume of the foam thereby providing access of the light to the photocatalyst supported on the pore walls of the foam. Thus, the goal of this work is the development of a high performance, structured photoreactor configuration capable of achieving significantly higher CO production rates than non-structured reactor systems (such as packed bed reactors, and thin films) through the Reverse Water Gas Shift (RWGS) reaction for the valorization of carbon dioxide:

$$CO_2 + H_2 \rightarrow CO + H_2O$$

At present, CO can be commercially obtained by means of the Methane Steam Reforming process and despite the high efficiency and

* Corresponding author at: Department of Chemistry, University of Toronto, 80 Saint George Street, ON, M5S 3H6, Toronto, Canada.
E-mail address: gozin@chem.utoronto.ca (G.A. Ozin).
[1] Current address: Unidad Académica Profesional Acolman, Universidad Autónoma del Estado de México, Camino de Caleros 11, 55875, Acolman, Mexico.
[2] These authors contributed equally to this work.

https://doi.org/10.1016/j.cej.2022.134864
Received 26 October 2021; Received in revised form 31 December 2021; Accepted 20 January 2022
Available online 25 January 2022

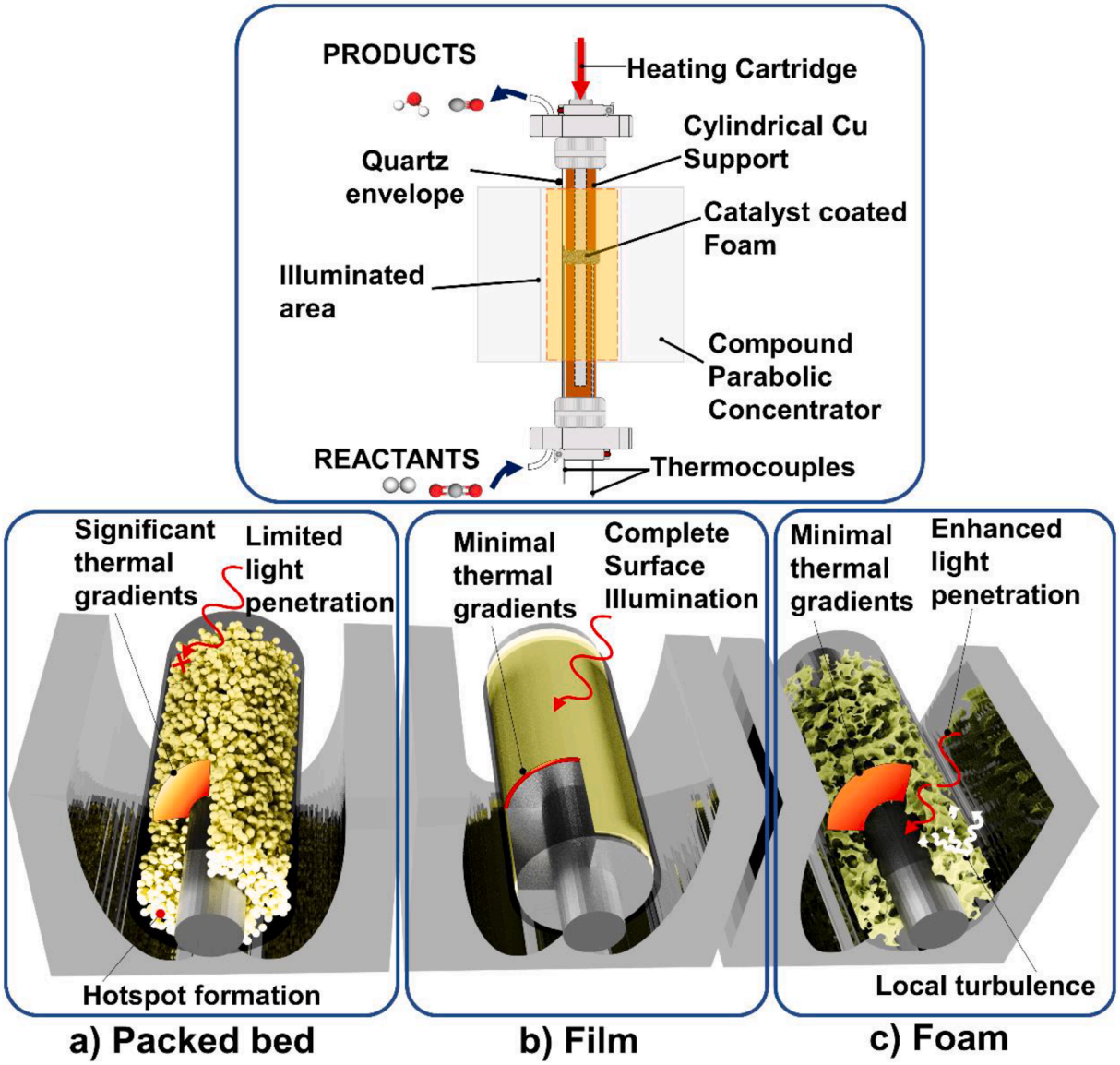

Fig. 1. Top: Simplified scheme of the annular photoreactor employed in this work to conduct the photo- and thermal CO_2 hydrogenation on coated foams. Bottom: Graphical representation of the physical phenomena involved in the RWGS process catalyzed by $In_2O_{3-x}(OH)_y$ nanorods under solar light for different reactor configurations: a) Packed bed, b) Thin film and c) coated foam.

cost-effectiveness of this method, significant challenges in the high energy requirements to reach elevated temperatures (700–900 °C) and stability reduction due to coke formation under these conditions remain. [5] In this context, the development of processes that require less aggressive reaction conditions and/or that are less reliant on fossil fuel-driven energy is necessary for future implementation at a large scale.

With the energy storage market expected to grow five-fold by 2040, [6] methanol produced via solar-driven RWGS is a potentially commercially viable energy storage solution (with appropriate carbon taxation) that leverages intermittently generated green hydrogen (forecasted price to drop below USD 1 kg^{-1} by 2030 [7,8]) and overcomes several challenges commonly associated with energy storage such as energy density, supply–demand responsiveness and transportability better than competing storage solutions. In order to realize this solution, however, a minimum 10% solar-to-fuel efficiency of the RWGS process is needed.[9] Successful pilot-scale deployment and benchmarking of lab-scale thermochemical RWGS catalysts that surpass commercial catalysts on a CO production rate versus CO cost metric, provides a useful point of comparison for new solar-driven RWGS photocatalyst candidate systems.

To achieve an optimal solar-to-fuel efficiency it is critical to use all the photons of the solar spectrum. Several recent review papers provide an excellent background on the thermodynamic and kinetic advantages as well as the several materials engineering approaches to maximize photothermal/photochemical enhancement of production rate and improving selectivity to the desired product particularly for CO_2 reduction.[10-17] A photo-thermal effect allows performing chemical reactions at relatively mild bulk conditions and is characterized by the synergy of the light absorption by the catalyst which leads to the generation of electron-hole pairs with the thermochemical processes simultaneously occurring at the catalytic surface either at a lower activation energy, higher local temperature or different mechanism to the photochemical process. This approach is promising given the continuous improvement possible at the nanoscale via materials engineering of photo-thermal properties of a catalyst system. For instance, the well-documented cubic indium oxide hydroxide ($In_2O_{3-x}(OH)_y$) provides opportunities to study the RWGS reaction driven either thermochemically or by hybrid photo- and thermal catalyst. [18]

As the nanorod $In_2O_{3-x}(OH)_y$ superstructure[19-21] is amenable for coating and has been shown to exhibit high activity and stability at temperatures up to 300 °C, this morphology was selected as an archetype for performing metallic foam (photo)catalyst experiments, in which the effects of both thermal and light input were tested.

In earlier studies, macroporous ceramic foams have been utilized as catalytic supports for solar thermochemical CO_2 conversion processes.[22-25] This approach uses high concentration solar irradiation to heat the catalytic foam to very high temperatures (1000–1500 °C). By contrast, in this work solar photochemical CO_2 conversion processes are driven by low concentration solar irradiation, under milder conditions on macroporous metallic foams. As a result, widely available, low cost solar concentrator equipment can be used with a smaller land footprint. Additionally, metallic photocatalytic foams have high thermal conductivity, are light weight and highly flexible, allowing straightforward shape control and facile incorporation into different photoreactor configurations. [26] Moreover, metallic foams offer a high ratio of active surface area to reactor volume, which is a desirable characteristic for a catalytic support and furthermore its high porosity ensures low pressure drops, lower pumping costs, improved catalyst-reactant interaction and efficient mass transfer in the reaction system. [27-29]

Foams with open cell and close cell structures with cell sizes ranging from 1 nm to over several mm are manufactured from materials that include copper, nickel, iron, titanium, alumina, silica, high performance plastics and carbon, and are commercially available at relatively low prices given their myriad industrial applications. Although several reports exist for the use of macroporous metallic foams as catalyst supports for CO_2 transformation processes,[30-35] they focus entirely on thermochemical CO_2 methanation and commonly performed in batch reactors. To the best of our knowledge, there is no prior work on photochemical CO_2 conversion, one of the main focuses of this work.

For this work, nickel foam was selected as the support for the $In_2O_{3-x}(OH)_y$ nanorods given the high thermal stability, commercial availability, and potential for surface chemical modification of Ni foam. The metallic support required surface pre-treatment before coating due to its low specific surface area (as low as 0.05 $m^2\ g^{-1}$ measured by BET analysis for commercial INCOFOAM nickel foam)[36] which would limit the amount of catalyst that could be supported. The $In_2O_{3-x}(OH)_y$ on Ni foams (with different pre-treatments) were integrated into a hybrid photothermal annular photoreactor[37] in which a hollow cylinder-shaped catalytic foam could be heated from the inside by an electrical heating cartridge and irradiated from the outside by a solar simulator, with the entire reactor assembly being mounted in a compound parabolic concentrator (Fig. 1 (top)).

Fig. 1 (top) illustrates the reactor employed in this work. Fig. 1 **(a)** presents a schematic representation of the phenomena occurring in a conventional packed catalyst bed. These include a higher likelihood of the occurrence of “hot spots” due to the unwanted heat distribution throughout the catalyst bed, contributing to deactivation of the catalyst and difficulties illuminating the catalytic particles located in the innermost part of the bed. In an earlier work, we presented the preparation and photocatalyst evaluation of $In_2O_{3-x}(OH)_y$ thin films, Fig. 1 **(b)**, in the reverse water gas shift (RWGS) process. While efficient light utilization was demonstrated with these thin film photocatalysts,[37] a large footprint would be required to achieve industrially useful conversions in a solar RWGS process.

Fig. 1 **(c)** depicts the physical processes occurring on the surface of the foam where a thin layer of nanostructured photocatalyst can be seen to facilitate molecular diffusion through efficient gas–solid contact. The interconnectedness and high thermal conductivity of the foam improves the uniformity of the heat distribution to and from the catalyst nanoparticles, whilst multiple light scattering-reflection events, internally throughout the macroporous structure increases the probability of light absorption.[38]

The key experimental variables include pre-treatment conditions of the Ni foam surface, reactant gas velocity, pore size and distribution of the foam and the process temperature. The CO production rate under thermal energy input only and the photochemical rate enhancement under additional illumination for the RWGS was used as the performance metrics of the system. Additionally, characterization of the $In_2O_{3-x}(OH)_y$ on the oxidized Ni foams before and after reaction provide information on the long-term stability of the catalyst. *In situ* DRIFTS results provide an insight into the effect of the metal foam support on the reaction pathway. The findings obtained in this work are expected to facilitate the development CO_2 photocatalytic foam enabled processes.

2. Materials and methods

2.1. Materials

Urea was obtained from Sigma-Aldrich. Anhydrous $InCl_3$ was purchased from Alfa Aesar, and methanol grade reagent were supplied by Fisher Scientific. All chemicals were used as received. Deionized water was used for the synthesis of the catalyst.

2.2. Catalyst synthesis and characterization

$In_2O_{3-x}(OH)_y$ nanorods were synthesized following the method reported previously by He et al.[21,20] In this procedure, 25 g of urea and 3 g of $InCl_3$ were dissolved in 100 mL of deionized water. The resulting solution was heated at 80 °C during 14 h under vigorous magnetic stirring. After this, the product was cooled down to room temperature, centrifuged and washed with deionized water. The white product ($In(OH)_3$) was dried at room temperature for 48 h and then calcined at 250 °C for 6 h under air atmosphere to obtain the final $In_2O_{3-x}(OH)_y$ rod-shaped superstructures. Characterization of the $In_2O_{3-x}(OH)_y$ superstructures was performed by PXRD and SEM. For this purpose, a Bruker D2-Phaser X-ray diffractometer was employed, using Cu Kα radiation at 30 kV and a FEI Quanta FEG 250 environmental SEM/STEM, respectively.

2.3. Foams coating and characterization

Nickel foam was supplied by Weijun Electronic Co. (China) with two different porosities: 110 ppi and 45 ppi corresponding to an average pore size of 0.2 and 1 mm, respectively. The thickness of the foam was 1.6 mm in all cases. Samples to be coated were cut out (6 cm length, 1 cm wide) and washed in an ultrasonic bath for 5 min. Samples were rinsed with deionized water and dried under vacuum for 2 h. In order to study the effect of the substrate on the quality of the coatings and on the CO_2 hydrogenation performance, three substrates were tested as a support for the $In_2O_{3-x}(OH)_y$ rod-shaped superstructures: metallic foam (MF), foam washed in acidic conditions (AF) to create surface roughness, and oxidized foam (OF), intended to create surface roughness and to increase surface area. MF was only washed as described before; AF was washed for 5 min in 0.1 M HCl in an ultrasonic bath, rinsed with deionized water and dried before coating; OF was calcined in air at 450 °C for six hours. The coating of the foam samples (MF, AF and OF) proceeded as follows: 50 mg of $In_2O_{3-x}(OH)_y$ nanorods were dispersed in 2.5 mL of a solvent mixture water: methanol (1:4) and sonicated in an ultrasonic bath for 20 min. The foam was weighed before coating and placed in a Petri dish with the catalyst dispersion for one minute. The sample was then removed from the dispersion, and the excess dispersion was removed from the pores of the foam by flowing air across the coated foam. The foam was further dried at 80 °C in a vacuum oven for 10 min before a next coating cycle. Unless stated in the text, this process was repeated twice, and the foam sample was bent into ring shape and dried at vacuum overnight. The mass of catalyst loaded onto each coated sample was determined as the difference between the dry bare foam (before coating) and the coated foam after drying employing for this purpose an analytical balance. The morphology of the surface of the coated foams samples was determined by SEM employing a FEI Quanta FEG 250

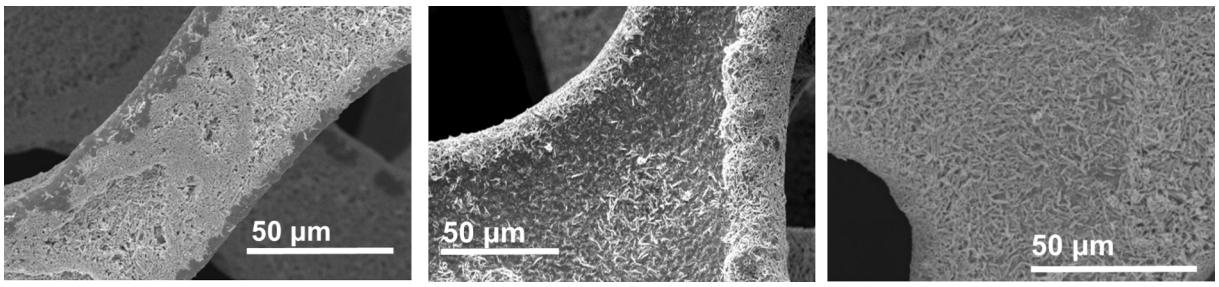

Fig. 2. Representative SEM images of coated samples using a different Ni substrate: a) Metallic nickel foam; b) Nickel foam washed in acidic media and c) oxidized nickel foam.

environmental SEM/STEM instrument. An X-ray computed tomography study was performed to a small section of the coated foam employing a micro–CT Skyscan1172 system. 39 keV and 248 µA initial current was the adopted conditions in this study. The 3D reconstruction process was performed through the software Image J. XPS measurements were performed using a Perkin Elmer Phi 5500 ESCA spectrometer in an ultra-high vacuum chamber with a base pressure of 1×10^{-9} Torr. The spectrometer uses an Al Kα X-ray source operating at 15 kV and 27 A.

2.4. CO_2 hydrogenation

The catalytic activity of the coated foams in the carbon dioxide hydrogenation process was evaluated in presence and absence of simulated sunlight. For this purpose, an annular reactor was employed, and it has been previously described in detail. [37] A detailed scheme of the reactor is presented in **Figure S3**. The inner cylinder corresponds to a copper rod (2.0 cm diameter) and the external cylinder is a quartz tube (2.2 cm internal diameter, 1 mm thickness). The coated foam to be tested was placed in the annular gap. The reactor length was 26 cm. The temperature of the reaction was controlled by an Omega temperature controller (model CN 7500) connected to a heating cartridge placed at the center of the reactor and connected to a K-type thermocouple placed on the surface of the tested foam. H_2 and CO_2 were fed to the system at a molar ratio 1:1. Hydrogen and CO_2 flowrates were controlled by a Brooks mass flow controller (model 5850S/BA) and an MKS Instruments mass flow controller (model 1139B-00050SV). Reaction products were periodically analyzed by gas chromatography employing a SRI 8610C instrument connected to the reaction system and configured with columns Hayesep D and Molsieve 5A. Argon was employed as carrier gas. Concentrations of the outlet gas stream components were determined by calibration performed with standards of known composition. Solar irradiation was replicated using a 3.5 kW solar simulator providing about 1.8 suns at the surface of the tested foams. Solar simulator was located in front of the annular reactor at a distance of 40 cm. Pre-treatment of the foam to be coated (metallic foam, foam washed in acidic conditions and oxidized foam), gas velocity (0–64 sccm), pore size of the foam (110 and 45 ppi), temperature (265 – 295 °C) and the simulated sunlight effect were evaluated in this work.

2.5. *In situ* DRIFTS study

In situ DRIFTS studies for the CO_2 hydrogenation on coated foams samples were conducted in a Thermo Scientific iS50 spectrometer equipped with a Harrick Praying Mantis DRIFT Accessory operating at a

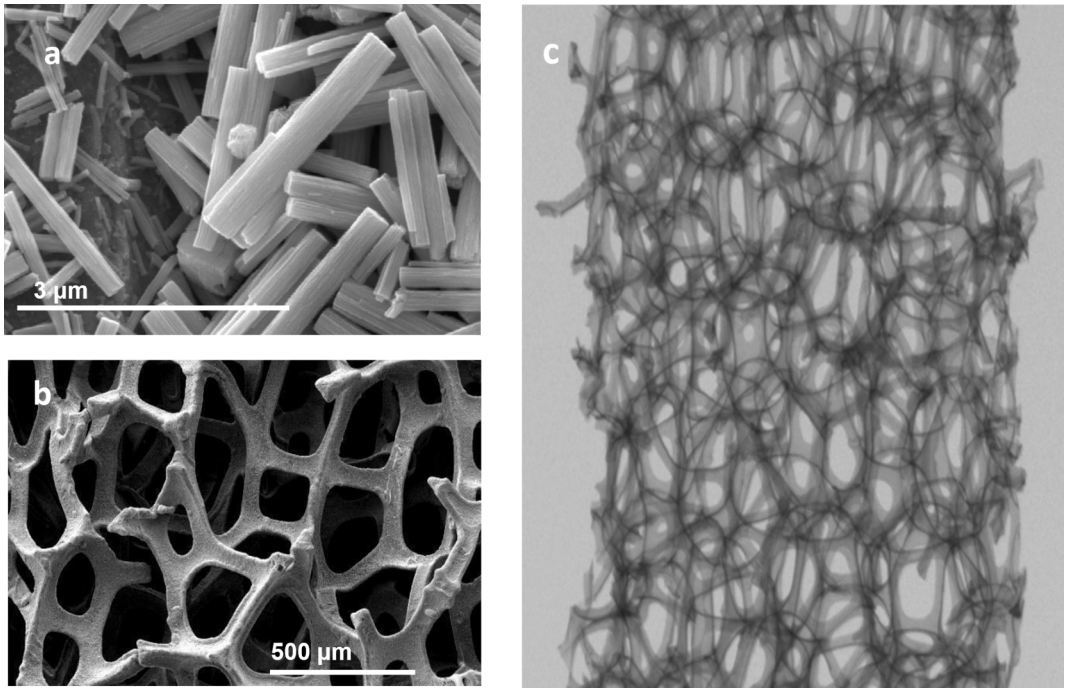

Fig. 3. SEM micrograph of a) $In_2O_{3-x}(OH)_y$ nanorods deposited on an individual strut of oxidized Ni foam, and b) Struts of oxidized Ni foam sample after coating process. c) 3D reconstruction of the coated foam acquired by X-ray computed tomography. The images correspond to oxidized nickel foam with pore density of 110 ppi (average pore size of 0.2 mm).

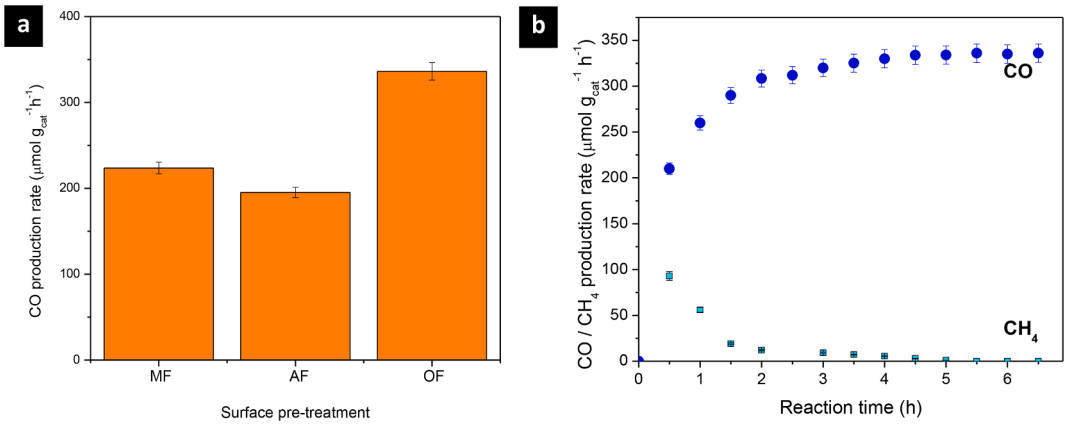

Fig. 4. CO_2 hydrogenation performance on coated Ni foams. **a)** CO production rate with coated foams: influence of the pre-treatment of the surface; **b)** Time evolution of the products of the gas phase RWGS process using an oxidized Ni foam coated with $In_2O_{3-x}(OH)_y$ catalyst (OF).

resolution of 2 cm^{-1}. The experiments were conducted at 150 °C since at higher temperatures it is not straightforward to obtain a high-quality signal due to the highly reflective properties of this catalyst. In each experiment the sample was initially purged with 15 sccm of Helium at room temperature for 30 min to remove impurities from the sample. First, the chamber was heated up to 150 °C and a background absorbance spectrum were collected. After this, H_2 was introduced to the chamber at a flow rate of 1 sccm followed by He to make up the total flow rate to 20 sccm, after which the absorbance spectra were collected. It must be noted that both the background and test spectra were taken at least twice to confirm measurements at the steady state. The same procedure was repeated separately for the measurements with mixtures of CO_2-He and H_2-CO_2-He gas atmospheres. The foam samples were adapted to fit into the sample holder.

3. Results

3.1. Effect of the substrate on coating and CO_2 hydrogenation performance

Rod-shaped nanocrystal $In_2O_{3-x}(OH)_y$ superstructures were synthesized, and the indium oxide phase was confirmed by matching the angular reflection in the acquired diffractogram with the PDF card 00–006-0416. The average length of the nanorods was verified to be 2.5 μm according to SEM imaging. The corresponding XRD pattern and representative SEM image are included as Supporting information (**Figure S1**). The specific surface area of the nanorods was reported to be 161.21 m^2 g^{-1} obtained from BET measurements. [21]

Regarding surface pre-treatment of the foams, three substrates were tested as support of the $In_2O_{3-x}(OH)_y$ rod-like superstructures. Representative images of the substrates before catalyst coating (**Figure S2**) and after two coating cycles (Fig. 2**)** are provided. Among the three coated foam samples, the OF sample was found to exhibit the most homogeneous and continuous layer of photocatalyst coated onto the porous structure. Superior affinity of the catalyst coating with the oxidized foam can be attributed to its higher hydrophilicity among the tested supports as well as the optimal surface wettability attained with the employed solvent mixture (water:methanol in ratio 1:4). In addition, the slow drying was beneficial for the strong adhesion of the catalyst to the walls of the foam. Representative SEM images and a 3D reconstruction of the coatings where OF was used, are presented in Fig. 3.

Fig. 3 **(a)** shows the continuous layer of nanorods deposited on the surface of the oxidized foam. No clogging of the pores is observed for the applied coating conditions, as verified by SEM (Fig. 3 **(b))** and a 3-D reconstruction of the foam from X-ray tomography cross-sectional images, Fig. 3 **(c).** Noteworthy here, is the uniformity of the coatings achieved by the simple method followed in this work using only small amounts of solvents to minimize residual carbon contamination on the catalyst. The deposition of a thin layer of catalyst is suitable for avoiding mass transfer limitations.

The catalytic activity of the three coated samples for the RWGS reaction was evaluated initially in dark conditions, under continuous operation of the annular reactor (shown in **Figure S3 (a)**). The reaction was performed at 275 °C with a total gas feed of 6 sccm composed of H_2 and CO_2 at a 1:1 M ratio to favor the RWGS. This process temperature was selected for evaluating coating stability at relatively high temperature reaction conditions. All reactor experiments to test the effect on coating stability and reaction products of the three different pre-treatment methods were conducted for 6 h. Carbon monoxide and methane were the only products that were detected. Under these reaction conditions, a stable CO production rate on the order of hundreds of micromoles, was observed for all three cases (Fig. 4 **(a)**). While CH_4 was produced, its rate decreased considerably during the first 2 h of reaction until it was no longer detected in the outlet gas stream. The highest CO production rate of 336 μmol CO $g_{cat}^{-1}h^{-1}$ was achieved by the oxidized foam sample, while the catalytic activity of the samples metallic nickel foam (MF) and nickel foam immersed in acid solution (AF) were both about 200 μmol CO $g_{cat}^{-1}h^{-1}$. Fig. 4 **(b)** shows the evolution of the reaction products when the oxidized foam sample was assessed. The difference in catalytic activity between the tested samples can be explained with the images included in Fig. 2**,** where it can be observed that part of the surface of MF and AF are not coated by nanorods leading to a lower catalytic activity. Both samples, MF and AF were loaded with 16 mg of catalyst after 2 coating cycles in contrast with the oxidized nickel foam (OF), where 23 mg of catalyst was loaded onto the foam. Due to the different loading of catalyst onto the foams surface (influenced by the properties of each sample), we report the CO production rate normalized per gram of catalyst. Additionally, the catalytic activity of the bare nickel foams samples for the RWGS reaction was assessed under identical reaction conditions as stated before. CO production was found to be negligible by testing MF and AF samples and for the case of OF, a CO production rate of 20 μmol CO $g_{cat}^{-1}h^{-1}$ was observed, only representing a small contribution to the total CO production achieved with the coated foam sample.

Prior to testing the coated foams under continuous operation, isotopic carbon dioxide ($^{13}CO_2$) hydrogenation tests on coated OF samples were conducted under total pressure of 30 psi in a batch reactor at 185 °C (maximum safe operational temperature of the reactor). By doing so, CO was confirmed to originate from $^{13}CO_2$, and not from residual carbon from the catalyst synthesis and/or coating process. In contrast, no ^{13}C-labelled CH_4 was detected, which indicates that methane detected at the beginning of the continuous flow experiment was residual from the synthesis or deposition procedure, rather than resulting from catalysis. Further details about the isotopic tests can be referred to

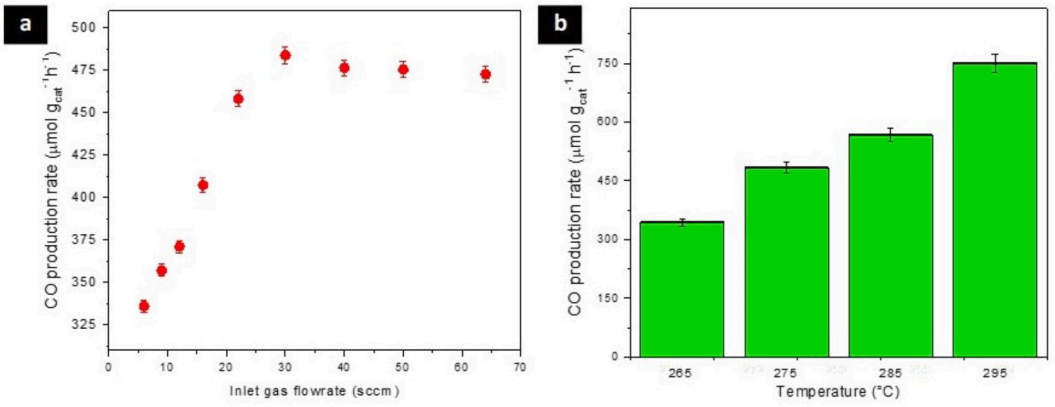

Fig. 5. a) CO production rate as function of the inlet gas flowrate. Reaction conditions: Temperature: 275 °C, CO_2:H_2 molar ratio 1:1, foam pore density of 110 ppi; b) CO_2 hydrogenation tested at different temperatures under continuous operation. Reaction conditions: Inlet gas flowrate: 30 sccm; CO_2:H_2 molar ratio 1:1, foam pore density of 110 ppi.

in the Supporting information (**Figure S4**).

3.2. Enhancement of mass and heat transfer in coated foams

The RWGS reaction was assessed at different conditions of temperature and gas flow (Fig. 5 **(a)** and Fig. 5 **(b)**), taking advantage of the negligible pressure drops and the negligible thermal gradients because of the thin layer of catalyst loaded onto the foam.

The CO production rate was measured as the inlet gas flow rate was varied, to identify the kinetic regime of the reaction, in which, there was maximal utilization of the reactant gases by the catalyst. The following inlet gas flowrates were assessed: 6, 9, 12, 16, 22, 30, 40, 50 and 64 sccm, composed of a 1:1 feed molar ratio of CO_2 to H_2. In all the cases, the selectivity towards CO was 100%. Trace amounts of methane was detected exclusively at the beginning of the reaction. Fig. 5 **(a)** presents the CO production rate as a function of the inlet gas flow rates fed to the reactor at 275 °C. The reactor operation under intrinsic kinetics was attained at an inlet gas flowrate of 30 sccm, where the highest CO production rate was reached. The graph shows that the CO production rate increases proportionally up to an inlet gas feed of 15 sccm of CO_2 and 15 sccm of H_2. At flow rates below 30 sccm, laminar flow dominated making it difficult for the adsorption/desorption processes involved in the effective transformation of CO_2 to CO to readily occur. In contrast, when the flow rate was faster than 30 sccm, the gas–solid contact time was likely too short and consequently not beneficial for the process, resulting in lower production of CO.

The influence of reaction temperature on the CO production rate and selectivity of the process was also evaluated. Experiments for the RWGS reaction were conducted using coated oxidized Ni foams. CO production rates plotted as a function of different temperatures (265, 275, 285 and 295 °C) are presented in Fig. 5 **(b)**. All experiments were performed under continuous flow (30 sccm) with CO as the only product detected. CO production increased from 332 μmol CO $g_{cat}^{-1}h^{-1}$ to 750 μmol CO $g_{cat}^{-1}h^{-1}$ when the temperature was increased from 265 to 295 °C. Stable production of CO was observed during at least 10 h (in extended experiments) without a drop in CO production rate. In addition, a pseudo-Arrhenius plot was prepared for estimation of the apparent activation energy for thermochemical CO_2 hydrogenation catalyzed by $In_2O_{3-x}(OH)_y$ deposited on a foam and thermochemically driven. The estimated value was 66 ± 0.17 kJ mol^{-1}.

3.3. Light utilization by photocatalytic foams

The coated foams were tested in the dark and under illumination between 265 and 295 °C in increments of 10 °C. Illumination was found to have a limited effect on rate enhancement at elevated temperatures

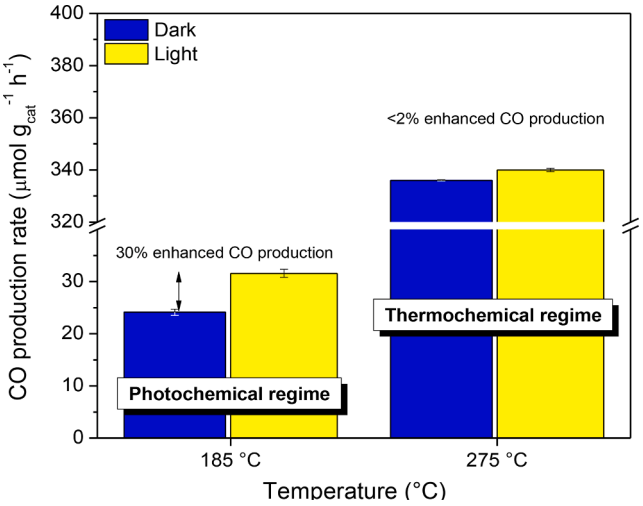

Fig. 6. CO production rate under dark and light conditions attained at different temperatures. Reaction conditions: Inlet flowrate: 6 sccm, CO_2:H_2 molar ratio 1:1; light intensity: 1.8 suns.

(less than 2% of enhancement in CO production rate due to light effect). Since the focus of the work is to demonstrate the photochemical rate enhancement capability of the foams as a macroporous structure and not modification of $In_2O_{3-x}(OH)_y$ to improve photochemical rate enhancement at higher temperatures, the coated foams were tested at 185 °C (as it was established to be an optimal temperature for photochemical rate enhancement under low concentration solar irradiation in previous work).[19,20] Also, it is important to note due to the exponential dependence of the CO production rate on temperature (as shown in Fig. 5 **(b)** and established in earlier reactor studies of cubic defected indium oxide [39]), a direct comparison cannot be made between production rates at the lower temperature (185 °C) and those at the higher temperature range (265–295 °C) in addition to the low concentration solar irradiation supplying a limited number of photons for photochemical work. Further, in this work, reactor testing was constraint to temperatures below 300 °C to be within the safe operating temperature limit of the reactor sealing components. Recent work demonstrating further improvement of the photochemical rate enhancement of defected indium oxide at higher temperature regimes through tunable synthesis of a polymorphic rhombohedral-cubic $In_2O_{3-x}(OH)_y$ and photothermal enhancement by extending the optical absorption range of the catalyst to utilize more of the solar spectrum by non-stoichiometrically reducing the indium oxide to a black form, can

Table 1
Summary of the photocatalytic performance of coated foams of different pore size to produce carbon monoxide. T = 185 °C; Inlet gas flowrate: 6 sccm; CO_2:H_2 molar ratio 1:1.

Foam density (ppi)	Average pore size (mm)	Mass of catalyst loaded (mg)	Foam coated area (cm^2)	% CO production rate improvement due to the sunlight	Selectivity to CO (%)	Quantum Yield (%)
110	0.2	15.2	49.7	30	81	0.00222
45	1.0	4.6	28.1	130	68	0.00428

Table 2
Summary of the photocatalytic performance of Indium-based catalyst assessed in different reactor configurations.

Material	Reactor configuration	H_2 /CO_2 Flow Rate (sccm H_2/sccm CO_2)	Temperature (°C)	Light Source	Main Product	Rate (μmol g^{-1} h^{-1})	Selectivity (%)
cubic-$In_2O_{3-x}(OH)_y$ nanocrystals[54]	Packed bed	3 sccm/ 3 sccm	150	300 W Xe lamp (22 suns)	CO	15	100
cubic-$In_2O_{3-x}(OH)_y$ nanorods[20]	Packed bed	6 sccm/ 2 sccm	300	130 W Xe lamp (~6 suns)	CH_3OH	205	50
rhombohedral-$In_2O_{3-x}(OH)_y$[40]	Packed bed	6 sccm/ 2 sccm	270	130 W Xe lamp (10 suns)	CH_3OH	180	13
$In_2O_{3-x}(OH)_y$ on Al rod [37]	Thin film	1 sccm/ 1 sccm	225	Solar simulator AM 1.5G (1.8 suns)	CO	49.6	100
$In_2O_{3-x}(OH)_y$ on Ni foam (This work)	Foam structured reactor	3 sccm/ 3 sccm	185	Solar simulator AM 1.5G (1.8 suns)	CO	32	81
$In_2O_{3-x}(OH)_y$ on Ni foam (This work)	Foam structured reactor	15 sccm/ 15 sccm	295	Solar simulator AM 1.5G (1.8 suns)	CO	755	100

allow better utilization of the foam advantages to show photochemical and photothermal rate enhancements at these high temperature regimes among other approaches to boost RWGS selectivity.[40-43]

Fig. 6 compares the effect of light to the RWGS reaction at different temperatures using coated foams. A significant light enhancement of the CO production rate was observed at this temperature under a reactor illumination intensity of 1.8 suns and an inlet gas flowrate of 6 sccm. The enhancement in CO production rate under light conditions was given by an increase from 24 to 32 μmol CO $g_{cat}^{-1}h^{-1}$ when the coated foams was irradiated with simulated sunlight. This increment represents an improvement of about 30% in comparison to the dark catalytic process. It must be noted that during all the experiments conducted at 185 °C there was no CO production when using bare nickel foams. Also, when the process was carried out below 200 °C, the selectivity towards CO was 81% with methane detected in the outlet stream unlike the experiment conducted at higher temperatures, where the selectivity towards CO after 6 h was 100%. In general, in our isotopic experiments, methane was not confirmed to originate from $^{13}CO_2$ and it can be assumed that residual carbon species on the surface of the coated foam are involved in such CH_4 production.

The effect of pore size (45 ppi and 110 ppi) on light enhancement for the RWGS was also studied. The CO production rates obtained in dark and light conditions for the two different pores are presented in Table 1, the CO production rate rises from 11 to 26 μmol CO $g_{cat}^{-1}h^{-1}$ when the foam with a larger pore size was tested under light. It means a 130% rate improvement due to the sunlight. Better light utilization by the foam with large pores can be explained by a larger fraction of the coated area being illuminated (almost 2-fold as shown in Table 1) as well as greater light scattering-reflection events provided by the random arrangement of the struts in the foams. In contrast, illumination of the catalyst layer on foams with narrow pores likely is unable to reach an extended coated area because of a shadow effect which may limit light penetration and absorption thoroughly. Quantum yield (QY) was estimated for both cases and it was determined a QY of 0.00428 and 0.00222 % for the pore densities of 45 and 110 ppi, respectively.

Selectivity towards CO was found to be dependent on the foam pore size. Differences in the amount of produced methane by samples of foam with different pore size can be explained by differences in the contact efficiency between the gas and the solid phase promoted by the macroscopic geometry of each foam.

The findings of the performance of the coated foams presented in this work are compared in Table 2 against similar CO_2 hydrogenation processes previously reported where different reactor configurations were employed. Even though a strict comparison between differences in reactor operation, gas flowrate and composition and morphology of the indium catalyst is not possible, this comparison is useful in contextualizing the advantages of coated foams and identifying opportunity areas for future studies.

The CO production rate achieved with the coated foams at 295 °C is higher than that of the other configurations in Table 2. This was largely possible to achieve due to higher inlet flow rates in the annular reactor (in comparison to the three first row, where a capillary channel was used). Also important is the absence of pressure drop when foams are employed. Likewise, in the present work the light intensity employed was considerably lower than in similar reports. Even with lower light intensity, we observed an enhancement of CO production rate when the coated foams were illuminated. Differences in selectivity are likely due to the different catalyst morphology and H_2/CO_2 ratio.

3.4. Catalyst-support interaction during CO_2 hydrogenation on foams

In this work utilization of hydroxylated indium oxide supported on a nickel substrate has been presented for the first time. Consequently, the interaction of the catalyst with the nickel oxide support was studied through XPS analysis and *in situ* DRIFTS experiments to evaluate the stability of the supported catalysis and to establish the reaction intermediates involved in the CO_2 conversion.

The obtained XPS spectra of the $In_2O_{3-x}(OH)_y$ on Ni foam sample before and after reaction are included in Fig. 7. The In $3d_{5/2}$ spectra is composed of non-symmetric peaks, in which the characteristic signal of indium oxide hydroxide has a binding energy of 444 eV. The peak was slightly displaced (0.2 eV) towards lower binding energy after reaction. For the Ni $2p_{3/2}$ spectra, the characteristic signal of NiO, the appearance of the split peak located at 853.8 eV and two satellite peaks at 861 eV and 880 eV can be observed in both samples although some minor changes were observed in the sample after reaction but without confirming the presence of additional Ni species to NiO. Lastly, for the O 1 s spectra, three oxygen species are distinguished by deconvolution of the spectra before reaction: indium oxide (530 eV), oxygen vacancies (531.7 eV) and surface OH groups (532.5 eV).[21] According to Chen et. al.,[44] this component has been associated with O^{2-} ions located in oxygen-deficient regions within the oxide matrix and as a result,

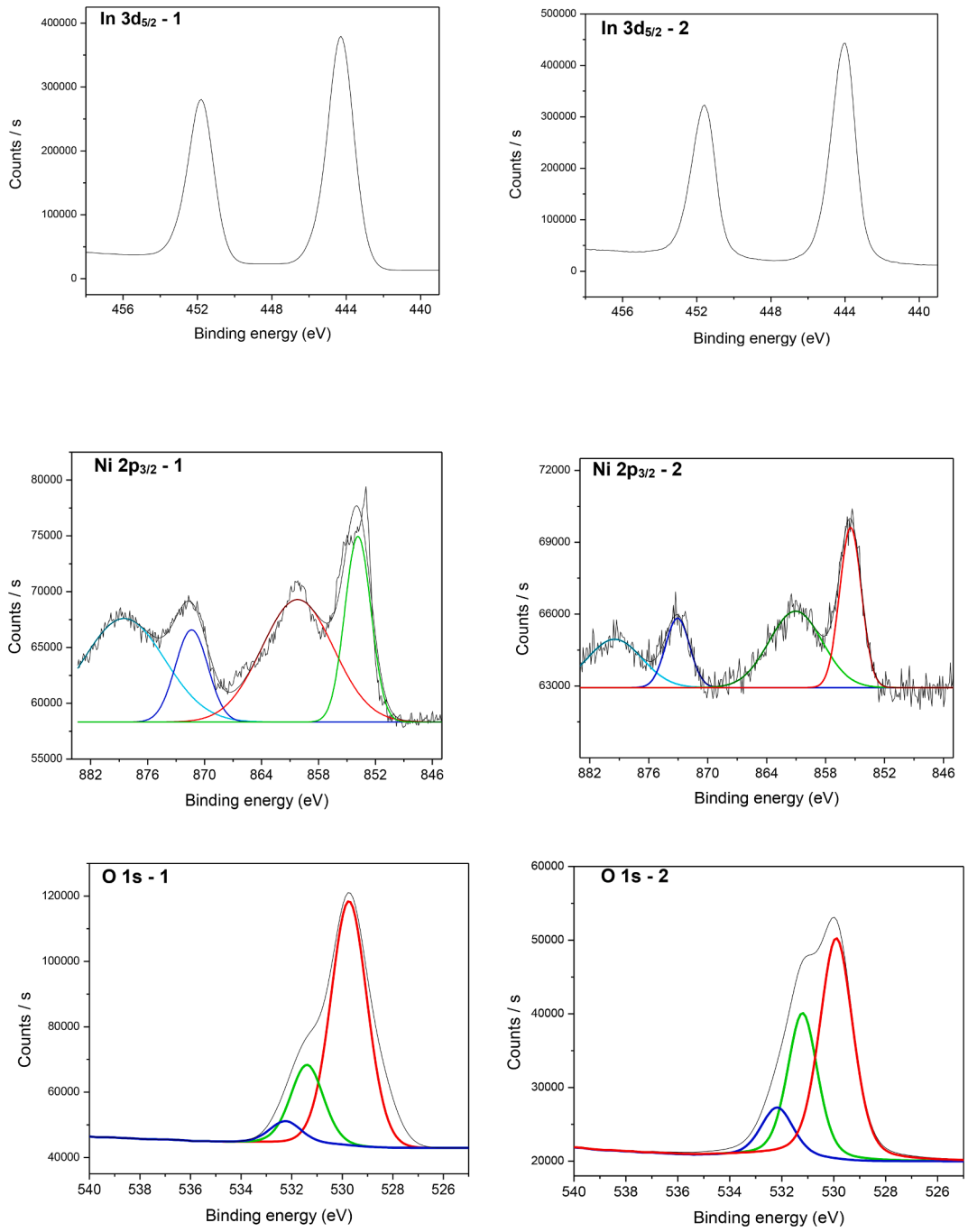

Fig. 7. XPS spectra of In $3d_{5/2}$, Ni $2p_{3/2}$ and O 1 s of $In_2O_{3-x}(OH)_y$ loaded on oxidized nickel foam before (left side) and after (right side) reaction.

"changes in the intensity of this component may be in connection with the variations in the concentration of the oxygen vacancies". The three oxygen species were present in both samples (before and after reaction) although changes in the ratio of the three oxygen species ratio were observed for the sample after reaction.

In situ DRIFTS experiments were performed under gas phase RWGS atmosphere with $In_2O_{3-x}(OH)_y$, to gain information about the role of the adsorbed species and its implication on activity and selectivity of the process. Two samples were under study: bare oxidized Ni foam and coated oxidized Ni foam. Fig. 8 presents the spectra obtained for each set of experiments.

According to the literature, the IR bands at 1230, 1442, and 1646 cm^{-1} are assigned to different vibrational modes of adsorbed bicarbonates,[45-47] while carbonate bands corresponds to 1336 cm^{-1} and 1525 cm^{-1} according to the same authors. Formate species are located at 1376, 1393 and 1593 cm^{-1}.[46] No adsorbed CO species were detected on the assessed samples (IR region about 2350 cm^{-1}).

The samples exposed to the gas stream containing H_2 and He (Fig. 8 **(a)**) did not show the presence of adsorbed species on the surface of bare oxidized foam and weak signals about 1435 cm^{-1} in the case of the coated foam. Conversely, when CO_2 balanced with He was introduced into the chamber (Fig. 8 **(b)**), chemical species were found to be adsorbed on the surface of the coated foam. The vibrational peaks identified at 1372 cm^{-1} are associated to formate species while bicarbonate was also identified at 1435 cm^{-1}. Bands located at 1511 and 1311 cm^{-1} correspond to additional adsorbed species not identified. There were no noticeable adsorbed species on the bare oxidized Ni foam.

Moreover, in the last set of experiments (Fig. 8 **(c)**), H_2, CO_2 and He

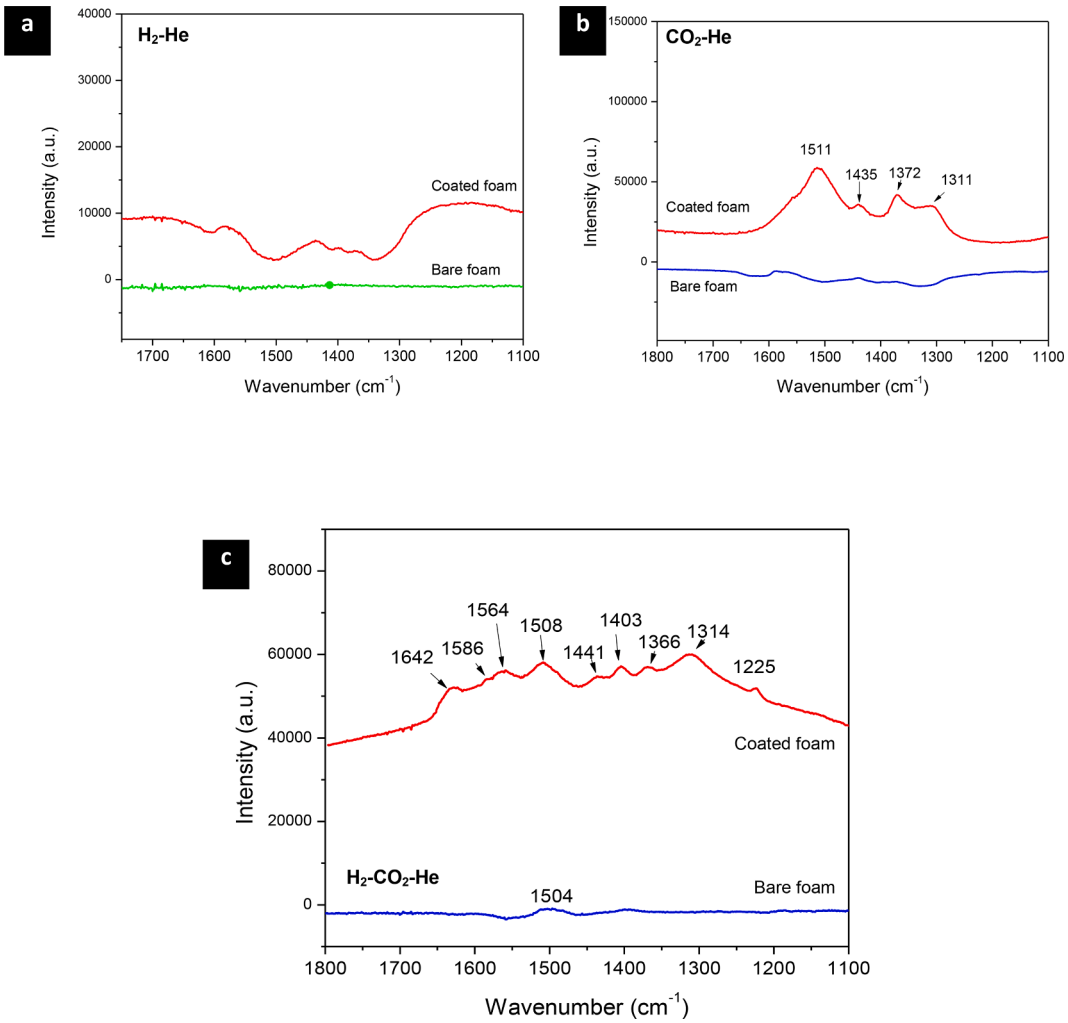

Fig. 8. *In situ* DRIFTS spectra of bare oxidized Ni foam and coated oxidized Ni foam obtained under different gas atmospheres at 150 °C. a) 1 sccm H_2 and 19 sccm He; b) 1 sccm CO_2 and 19 sccm He; c) 1 sccm H_2, 1 sccm CO_2 and 18 sccm He.

were fed to mimic the actual gas phase RWGS process. The bare oxidized Ni foam did not seem to have strong interaction with the gas phase whilst in the coated foam sample bicarbonate and carbonate were clearly identified (1225, 1441 and 1642 cm^{-1}), and the bands located at 1366 and 1403 cm^{-1} likely correspond to formate adsorbed species.

4. Discussion

The utilization of metallic foams as catalyst support was beneficial for achieving efficient mass transfer by engineering an alternative reactor configuration to the traditional packed bed in the evaluation of nanostructured rod-like $In_2O_{3-x}(OH)_y$ catalyst. Gas flow rates up to 64 sccm were processed to convert CO_2 to CO in the annular reactor using coated foams. This represents a step forward to the design of pilot scale processes for conversion of CO_2 by photochemical processes. It is important to highlight the relevance of the random structures of the metallic foams; the gas stream is diverted through the interconnected channels which acts as static mixer generating turbulence.[48] Also, despite the relatively large flow rates passing through the reactor, no pressure drop was detected in the system because of the high porosity of the foams, which is particularly beneficial for the safety of the process at larger scale.

Several studies have well documented the strong photoresponse of $In_2O_{3-x}(OH)_y$ catalyst and our results confirmed this feature for a delimited interval of temperatures despite the size of the foam: below 200 °C, the photochemical effect had a more pronounced impact on the CO_2 conversion in comparison to process temperatures close to 300 °C. The limited effect of illumination on rate enhancement at elevated temperatures (less than 2% of enhancement in CO production rate due to light effect) is attributable to a higher rate of non-radiative multi-phonon relaxation competing with electron-hole separation enabling chemistry, a phenomenon commonly observed in semiconductor materials at higher temperatures.[49,50] Our findings suggest that in the RWGS process catalyzed by $In_2O_{3-x}(OH)_y$ coated foams a synergy exists between the light driven reaction and the thermally activated process and the dominant mechanism (photochemical / thermochemical) is directly linked to the temperature at which the experiment is being carried out. Elsewhere, it was demonstrated that the foam dimension is determinant for a better penetration of the light through the reactor.

Selectivity of our RWGS process differs from previous reports for this catalyst. Methane was not quantified before in contrast to methanol, which in our experiment was detected only in trace amount. This is not surprising since we introduce the variable of oxidized nickel foam. At specific temperatures (for example, below 200 °C) the occurrence of parallel reactions to the RWGS process are likely. Namely, the CO_2 methanation reaction and CO methanation process, which have been reported to have been promoted by Ni species.[51-53] To provide further evidence of the role of Ni species, XPS and DRIFTS studies were carried out. From XPS, we can extract that in our study, changes in the amount of oxygen vacancies and OH groups after reaction are attributed

to the high mobility of charge carriers induced by the presence of Ni species. A surface rich in electrons created through the oxygen vacancies strongly binds the OH groups with In, generating the active surface site. This active site promotes the heterolytic splitting of H_2 for the subsequent adsorption and dissociation of CO_2 releasing CO as reaction product. According to DRIFTS, CO_2 hydrogenation proceeds through bicarbonate, carbonate, and formate species, but the unidentified peaks at 1314, 1508, 1564 and 1586 cm^{-1}, suggest that additional different adsorbed species are also involved in the reaction pathway when coated foams are employed

5. Conclusion

Indium oxide hydroxide nanorods were successfully coated on an oxidized nickel foam ($In_2O_{3-x}OH_y$ on Ni) and its reverse water gas shift thermochemical and photochemical activity were assessed in a hybrid photo- and thermal catalytic annular reactor. The process was optimized through variations in the surface structure, composition and pore size of the foam and the inlet gas flowrate and temperature of the process. A light-enhanced CO production rate up to 130% was achieved through enhanced light penetration and a remarkably high thermochemical CO production rate at 295 °C of 0.75 mmol g_{cat}^{-1} h^{-1} was achieved under continuous operation conditions. The challenges of developing photocatalysts and photoreactors that efficiently facilitate mass, heat, and light transfer to enable gas-phase heterogeneous CO_2 hydrogenation reactions are substantial. Whilst, there are orders of magnitude gaps to be bridged between defected indium oxide and commercial Cu/ZnO/Al_2O_3 when it comes to the CO production versus cost of CO production metric (refer to Table S1 in supporting information) the approximately one order of magnitude improvement in the CO production rate for the $In_2O_{3-x}OH_y$ nanorods coated on foams compared to that of the-packed bed and thin film configurations can play an important role in partly improving the catalyst utilization and viability (Table 2). The results and learning described in this study augur well for the accelerated development of solar fuels science to achieve technology readiness levels that can enable the industrialization of gas-phase heterogeneous CO_2 photocatalysis.

Author Contributions

L.H., A.M., U.U., M.M.S, G.A.O and R.N. conceived and designed the experiments. L.H. and A.M. carried out the synthesis of the materials, tested different coating methods, performed coated foams characterizations, and carried out the experiments in the annular reactor. G.A.O. and M.S. funded the project. G.A.O. supervised the project. L.H., A.M and G.A.O. wrote the paper. W.S., L.W. K.B. and A.T. provide significant contributions to the discussion. All the authors discussed the results and commented on the manuscript.

Declaration of Competing Interest

The authors declare that they have no known competing financial interests or personal relationships that could have appeared to influence the work reported in this paper.

Acknowledgements

GAO is Government of Canada Research Chair. He acknowledges the financial support of the Ontario Ministry of Research and Innovation (MRI), the Ministry of Economic Development, Employment and Infrastructure (MEDI), the Ministry of the Environment and Climate Change's (MOECC) and the Best in Science (BIS) Award. Acknowledged is additional support from the Ontario Center of Excellence (OCE) Solutions 2030 Challenge Fund, the Low Carbon Innovation Fund (LCIF), Imperial Oil, University of Toronto Connaught Innovation Fund (CIF), University of Toronto Connaught Global Challenge (CGC) Fund, the Natural Sciences and Engineering Research Council of Canada (NSERC) and J. Tjong of Ford Motor Canada. L.H. acknowledges the support of the Postdoctoral Fellowship SECITI (066/2017). W.S. acknowledges the ZJU100 Young Professor Program, and the NSFC (Grant No. 51902287). The authors gratefully acknowledge Meikun Xia and Christian Belachew for XPS and X-ray computed tomography studies, respectively.

Appendix. . A supplementary data

Characterization of the $In_2O_{3-x}(OH)_y$ rod-shaped superstructures (XRD and SEM), SEM images of the pre-treated nickel foam samples (bare and coated samples), annular reactor schematics, ^{13}C experiments with coated foams in a batch reactor, and quantum yield of coated foam.

Appendix A. Supplementary data

Supplementary data to this article can be found online at https://doi.org/10.1016/j.cej.2022.134864.

References

[1] G. Centi, S. Perathoner, Opportunities and prospects in the chemical recycling of carbon dioxide to fuels, Catal. Today. 148 (3-4) (2009) 191–205.
[2] M. Peters, B. Köhler, W. Kuckshinrichs, W. Leitner, P. Markewitz, T.E. Müller, Chemical technologies for exploiting and recycling carbon dioxide into the value chain, ChemSusChem. 4 (9) (2011) 1216–1240, https://doi.org/10.1002/cssc.201000447.
[3] G.A. Olah, A. Goeppert, G.K.S. Prakash, Chemical recycling of carbon dioxide to methanol and dimethyl ether: from greenhouse gas to renewable, environmentally carbon neutral fuels and synthetic hydrocarbons, J. Org. Chem. 74 (2) (2009) 487–498, https://doi.org/10.1021/jo801260f.
[4] B. Hu, C. Guild, S.L. Suib, Thermal, electrochemical, and photochemical conversion of CO_2 to fuels and value-added products, J. CO2 Util. 1 (2013) 18–27, https://doi.org/10.1016/J.JCOU.2013.03.004.
[5] M.B. Syed, Technologies for renewable hydrogen production, Bioenergy Resour. Technol. (2021) 157–198, https://doi.org/10.1016/B978-0-12-822525-7.00013-5.
[6] Energy Storage is a $620 Billion Investment Opportunity to 2040 | BloombergNEF. https://about.bnef.com/blog/energy-storage-620-billion-investment-opportunity-2040/ (accessed December 30, 2021).
[7] BloombergNEF, Hydrogen Economy Outlook Key messages, (2020). https://data.bloomberglp.com/professional/sites/24/BNEF-Hydrogen-Economy-Outlook-Key-Messages-30-Mar-2020.pdf (accessed December 30, 2021).
[8] Experts explain why green hydrogen costs have fallen and will keep falling | S&P Global Market Intelligence. https://www.spglobal.com/marketintelligence/en/news-insights/latest-news-headlines/experts-explain-why-green-hydrogen-costs-have-fallen-and-will-keep-falling-63037203 (accessed December 30, 2021).
[9] A.A. Tountas, G.A. Ozin, M.M. Sain, Solar methanol energy storage, Nat. Catal. 4 (11) (2021) 934–942, https://doi.org/10.1038/s41929-021-00696-w.
[10] M. Ghoussoub, M. Xia, P.N. Duchesne, D. Segal, G. Ozin, Principles of photothermal gas-phase heterogeneous CO_2 catalysis, Energy Environ. Sci. 12 (4) (2019) 1122–1142, https://doi.org/10.1039/C8EE02790K.
[11] I. Barba-Nieto, N. Gómez-Cerezo, A. Kubacka, M. Fernández-García, Oxide-based composites: applications in thermo-photocatalysis, Catal, Sci. Technol. 11 (21) (2021) 6904–6930, https://doi.org/10.1039/D1CY01067K.
[12] R. Ma, J. Sun, D.H. Li, J.J. Wei, Review of synergistic photo-thermo-catalysis: Mechanisms, materials and applications, Int. J. Hydrogen Energy. 45 (55) (2020) 30288–30324.
[13] A. Francis, S.P. S., H.K. S, S. K, M. Tahir, A review on recent developments in solar photoreactors for carbon dioxide conversion to fuels, J. CO2 Util. 47 (2021) 101515.
[14] D. Mateo, J.L. Cerrillo, S. Durini, J. Gascon, Fundamentals and applications of photo-thermal catalysis, Chem. Soc. Rev. 50 (3) (2021) 2173–2210, https://doi.org/10.1039/D0CS00357C.
[15] M. Sun, B. Zhao, F. Chen, C. Liu, S. Lu, Y. Yu, B. Zhang, Thermally-assisted photocatalytic CO_2 reduction to fuels, Chem. Eng. J. 408 (2021) 127280.
[16] M. Gao, L. Zhu, C.K. Peh, G.W. Ho, Solar absorber material and system designs for photothermal water vaporization towards clean water and energy production. Energy Environ. Sci. 12 (3) (2019) 841–864, https://doi.org/10.1039/C8EE01146J.
[17] Z.-J. Wang, H. Song, H. Liu, J. Ye, Coupling of solar energy and thermal energy for carbon dioxide reduction: status and prospects, Angew. Chemie Int. Ed. 59 (21) (2020) 8016–8035.
[18] K.K. Ghuman, T.E. Wood, L.B. Hoch, C.A. Mims, G.A. Ozin, C.V. Singh, Illuminating CO_2 reduction on frustrated Lewis pair surfaces: Investigating the role of surface hydroxides and oxygen vacancies on nanocrystalline $In_2O_{3-x}(OH)_y$, Phys. Chem. Chem. Phys. 17 (2015) 14623–14635, https://doi.org/10.1039/c5cp02613j.
[19] L.U. Wang, M. Cai, W. Sun, L.E. He, X. Zhang, Promoting charge separation in semiconductor nanocrystal superstructures for enhanced photocatalytic activity,

Adv. Mater. Interfaces. 5 (13) (2018) 1701694, https://doi.org/10.1002/admi.201701694.
[20] L.E. He, T.E. Wood, B.o. Wu, Y. Dong, L.B. Hoch, L.M. Reyes, D.I. Wang, C. Kübel, C. Qian, J. Jia, K. Liao, P.G. O'Brien, A. Sandhel, J.Y.Y. Loh, P. Szymanski, N. P. Kherani, T.C. Sum, C.A. Mims, G.A. Ozin, Spatial separation of charge carriers in $In_2O_{3-x}(OH)_y$ nanocrystal superstructures for enhanced gas-phase photocatalytic activity, ACS Nano. 10 (5) (2016) 5578–5586, https://doi.org/10.1021/acsnano.6b0234610.1021/acsnano.6b02346.s001.
[21] L.u. Wang, M. Ghoussoub, H. Wang, Y. Shao, W. Sun, A.A. Tountas, T.E. Wood, H. Li, J.Y.Y. Loh, Y. Dong, M. Xia, Y. Li, S. Wang, J. Jia, C. Qiu, C. Qian, N. P. Kherani, L.E. He, X. Zhang, G.A. Ozin, Photocatalytic hydrogenation of carbon dioxide with high selectivity to methanol at atmospheric pressure, Joule. 2 (7) (2018) 1369–1381.
[22] S. Lorentzou, D. Dimitrakis, A. Zygogianni, G. Karagiannakis, A. G. Konstandopoulos, Thermochemical H_2O and CO_2 splitting redox cycles in a $NiFe_2O_4$ structured redox reactor: Design, development and experiments in a high flux solar simulator, Sol. Energy. 155 (2017) 1462–1481, https://doi.org/10.1016/J.SOLENER.2017.07.001.
[23] P. Furler, J. Scheffe, M. Gorbar, L. Moes, U. Vogt, A. Steinfeld, Solar thermochemical CO_2 splitting utilizing a reticulated porous ceria redox system, Energy and Fuels. 26 (11) (2012) 7051–7059, https://doi.org/10.1021/ef3013757.
[24] M.M. Nair, S. Abanades, Tailoring hybrid nonstoichiometric ceria redox cycle for combined solar methane reforming and thermochemical conversion of H_2O/CO_2, Energy and Fuels. 30 (7) (2016) 6050–6058, https://doi.org/10.1021/acs.energyfuels.6b0106310.1021/acs.energyfuels.6b01063.s001.
[25] S. Bhatta, D. Nagassou, S. Mohsenian, J.P. Trelles, Photo-thermochemical decomposition of carbon-dioxide in a direct solar receiver-reactor, Sol. Energy. 178 (2019) 201–214, https://doi.org/10.1016/J.SOLENER.2018.12.019.
[26] F. García-Moreno, Francisco, commercial applications of metal foams: their properties and production, Materials (Basel). 9 (2016) 85, https://doi.org/10.3390/ma9020085.
[27] A. Montebelli, C.G. Visconti, G. Groppi, E. Tronconi, S. Kohler, H.J. Venvik, R. Myrstad, Washcoating and chemical testing of a commercial $Cu/ZnO/Al_2O_3$ catalyst for the methanol synthesis over copper open-cell foams, Appl. Catal. A Gen. 481 (2014) 96–103, https://doi.org/10.1016/j.apcata.2014.05.005.
[28] A. Montebelli, C.G. Visconti, G. Groppi, E. Tronconi, C. Cristiani, C. Ferreira, S. Kohler, Methods for the catalytic activation of metallic structured substrates, Catal, Sci. Technol. 4 (9) (2014) 2846–2870, https://doi.org/10.1039/C4CY00179F.
[29] L. Giani, G. Groppi, E. Tronconi, Mass-transfer characterization of metallic foams as supports for structured catalysts, Ind. Eng. Chem. Res. 44 (14) (2005) 4993–5002, https://doi.org/10.1021/ie0490886.
[30] H.C. Wu, Y.C. Chang, J.H. Wu, J.H. Lin, I.K. Lin, C.S. Chen, Methanation of CO_2 and reverse water gas shift reactions on Ni/SiO_2 catalysts: the influence of particle size on selectivity and reaction pathway, Catal, Sci. Technol. 5 (8) (2015) 4154–4163.
[31] A. Vita, C. Italiano, L. Pino, P. Frontera, M. Ferraro, V. Antonucci, Activity and stability of powder and monolith-coated Ni/GDC catalysts for CO_2 methanation, Appl. Catal. B Environ. 226 (2018) 384–395, https://doi.org/10.1016/J.APCATB.2017.12.078.
[32] Z. Liang, P. Gao, Z. Tang, M. Lv, Y. Sun, Three dimensional porous Cu-Zn/Al foam monolithic catalyst for CO2 hydrogenation to methanol in microreactor, J. CO2 Util. 21 (2017) 191–199, https://doi.org/10.1016/J.JCOU.2017.05.023.
[33] Y. Li, Q. Zhang, R. Chai, G. Zhao, Y.e. Liu, Y. Lu, F. Cao, $Ni-Al_2O_3$/Ni-foam catalyst with enhanced heat transfer for hydrogenation of CO2 to methane, AIChE J. 61 (12) (2015) 4323–4331, https://doi.org/10.1002/aic.14935.
[34] M. Frey, D. Édouard, A.-C. Roger, Optimization of structured cellular foam-based catalysts for low-temperature carbon dioxide methanation in a platelet milli-reactor, Comptes Rendus Chim. 18 (3) (2015) 283–292.
[35] M. Frey, A. Bengaouer, G. Geffraye, D. Edouard, A.-C. Roger, Aluminum open cell foams as efficient supports for carbon dioxide methanation catalysts: pilot-scale reaction results, Energy Technol. 5 (11) (2017) 2078–2085, https://doi.org/10.1002/ente.201700188.
[36] X. Huang, G. Franchi, F. Cai, Characterization of porous bi-modal Ni structures, J. Porous Mater. 16 (2) (2009) 165–173, https://doi.org/10.1007/s10934-007-9181-8.
[37] A. Mohan, U. Ulmer, L. Hurtado, J. Loh, Y.F. Li, A.A. Tountas, C. Krevert, C. Chan, Y. Liang, P. Brodersen, M.M. Sain, G.A. Ozin, A hybrid photo- and thermal catalyst system for continuous CO_2 reduction, ACS Appl, Mater. Interfaces. 12 (30) (2020) 33613–33620, https://doi.org/10.1021/acsami.0c0623210.1021/acsami.0c06232.s001.
[38] Y. Li, X.-L. Xia, Q. Ai, C. Sun, H.-P. Tan, Pore-level determination of spectral reflection behaviors of high-porosity metal foam sheets, Infrared Phys. Technol. 89 (2018) 77–87, https://doi.org/10.1016/J.INFRARED.2017.12.016.
[39] K.K. Ghuman, T.E. Wood, L.B. Hoch, C.A. Mims, G.A. Ozin, C.V. Singh, Illuminating CO_2 reduction on frustrated Lewis pair surfaces: investigating the role of surface hydroxides and oxygen vacancies on nanocrystalline $In_2O_{3-x}(OH)_y$, Phys. Chem. Chem. Phys. 17 (22) (2015) 14623–14635, https://doi.org/10.1039/C5CP02613J.
[40] T. Yan, L. Wang, Y. Liang, M. Makaremi, T.E. Wood, Y. Dai, B. Huang, A.A. Jelle, Y. Dong, G.A. Ozin, Polymorph selection towards photocatalytic gaseous CO2 hydrogenation, Nat. Commun. 10 (2019) 2521, https://doi.org/10.1038/s41467-019-10524-2.
[41] L. Wang, Y. Dong, T. Yan, Z. Hu, A.A. Jelle, D.M. Meira, P.N. Duchesne, J.Y.Y. Loh, C. Qiu, E.E. Storey, Y. Xu, W. Sun, M. Ghoussoub, N.P. Kherani, A.S. Helmy, G. A. Ozin, Black indium oxide a photothermal CO2 hydrogenation catalyst, Nat. Commun. 11 (2020) 2432, https://doi.org/10.1038/s41467-020-16336-z.
[42] Y. Dong, P. Duchesne, A. Mohan, K.K. Ghuman, P. Kant, L. Hurtado, U. Ulmer, J.Y. Y. Loh, A.A. Tountas, L. Wang, A. Jelle, M. Xia, R. Dittmeyer, G.A. Ozin, Shining light on CO_2: from materials discovery to photocatalyst, photoreactor and process engineering, Chem. Soc. Rev. 49 (2020) 5648–5663, https://doi.org/10.1039/D0CS00597E.
[43] W. Wang, Y. Zhang, Z. Wang, J.M. Yan, Q. Ge, C.J. Liu, Reverse water gas shift over In_2O_3–CeO_2 catalysts, Catal. Today. 259 (2016) 402–408, https://doi.org/10.1016/J.CATTOD.2015.04.032.
[44] P.-T. Hsieh, Y.-C. Chen, K.-S. Kao, C.-M. Wang, Luminescence mechanism of ZnO thin film investigated by XPS measurement, Appl. Phys. A Mater. Sci. Process. 90 (2) (2007) 317–321, https://doi.org/10.1007/s00339-007-4275-3.
[45] T. Das, G. Deo, Synthesis, characterization and in situ DRIFTS during the CO2 hydrogenation reaction over supported cobalt catalysts, J. Mol. Catal. A Chem. 350 (1-2) (2011) 75–82, https://doi.org/10.1016/j.molcata.2011.09.008.
[46] X. Wang, H. Shi, J.H. Kwak, J. Szanyi, Mechanism of CO2 Hydrogenation on Pd/Al_2O_3 Catalysts: Kinetics and Transient DRIFTS-MS Studies, ACS Catal. 5 (11) (2015) 6337–6349, https://doi.org/10.1021/acscatal.5b01464.
[47] J.C.S. Wu, C.-W. Huang, In situ DRIFTS study of photocatalytic CO2 reduction under UV irradiation, Front. Chem. Eng. China. 4 (2) (2010) 120–126, https://doi.org/10.1007/s11705-009-0232-3.
[48] J. Gascon, J.R. van Ommen, J.A. Moulijn, F. Kapteijn, Structuring catalyst and reactor - An inviting avenue to process intensification, Catal, Sci. Technol. 5 (2) (2015) 807–817.
[49] S. Linic, U. Aslam, C. Boerigter, M. Morabito, Photochemical transformations on plasmonic metal nanoparticles, Nat. Mater. 14 (6) (2015) 567–576, https://doi.org/10.1038/nmat4281.
[50] P. Christopher, H. Xin, A. Marimuthu, S. Linic, Singular characteristics and unique chemical bond activation mechanisms of photocatalytic reactions on plasmonic nanostructures, Nat. Mater. 11 (12) (2012) 1044–1050, https://doi.org/10.1038/nmat3454.
[51] H. Wang, K.E. Xu, X. Yao, D. Ye, Y. Pei, H. Hu, M. Qiao, Z.H. Li, X. Zhang, B. Zong, Undercoordinated site-abundant and tensile-strained nickel for low-temperature CO_x methanation, ACS Catal. 8 (2) (2018) 1207–1211, https://doi.org/10.1021/acscatal.7b0294410.1021/acscatal.7b02944.s001.
[52] R. Zhou, N. Rui, Z. Fan, C.-J. Liu, Effect of the structure of Ni/TiO2 catalyst on CO2 methanation, Int. J. Hydrogen Energy. 41 (47) (2016) 22017–22025.
[53] T.A. Le, M.S. Kim, S.H. Lee, T.W. Kim, E.D. Park, CO and CO2 methanation over supported Ni catalysts, Catal. Today. 293-294 (2017) 89–96.
[54] L.B. Hoch, T.E. Wood, P.G. O'Brien, K. Liao, L.M. Reyes, C.A. Mims, G.A. Ozin, The rational design of a single-component photocatalyst for gas-phase CO_2 reduction using both UV and visible light, Adv. Sci. 1 (1) (2014) 1400013, https://doi.org/10.1002/advs.201400013.